

# **Transmutation, gas production, and helium embrittlement in materials under neutron irradiation.**

**M.R. Gilbert, S.L. Dudarev, S. Zheng, L.W. Packer, and  
J.-Ch. Sublet**

EURATOM/CCFE Fusion Association, Culham Centre for Fusion Energy,  
Abingdon, Oxfordshire OX14 3DB, UK.

E-mail: [mark.gilbert@ccfe.ac.uk](mailto:mark.gilbert@ccfe.ac.uk)

**Abstract.** The high-energy, high-intensity neutron fluxes produced by the fusion plasma will have a significant life-limiting impact on reactor components in both experimental and commercial fusion devices. As well as producing defects, the neutrons bombarding the materials initiate nuclear reactions, leading to transmutation of the elemental atoms. Products of many of these reactions are gases, particularly helium and hydrogen, which cause swelling and embrittlement of materials. This paper investigates, using both neutron-transport and inventory calculations, the variation in nuclear transmutation and gas production rates at various locations of a conceptual design of the next-step fusion device DEMO. Modelling of grain structures and gas diffusion rates illustrates that the timescale for susceptibility to helium embrittlement varies widely between different materials, and between the same materials situated at different locations in the DEMO structure.

## 1. Introduction

In magnetic-confinement fusion reactors a large number of high-energy neutrons are generated in the plasma by deuterium-tritium fusion reactions. These neutrons escape from the plasma and irradiate the materials that make up the reactor vessel. One of the key outstanding issues for fusion research is in the understanding of how neutrons impact on the properties of materials. Not only do the incident neutrons cause atomic displacements within the materials, leading to defect generation and accumulation, but they also initiate non-elastic nuclear reactions that alter the nature of the constituent atoms. This process, known as transmutation or burn-up, changes the chemical composition of materials, leading in turn to measurable changes in structural and mechanical properties.

Perhaps even more problematic are the nuclear reactions initiated by fusion neutrons that give rise to the transmutation production of gas atoms, such as helium (He) and hydrogen (H). These reactions, which include neutron capture followed by  $\alpha$ -particle ( ${}^4\text{He}^{2+}$ ) emission, often written as  $(n, \alpha)$ , and neutron capture and proton ( ${}^1\text{H}^+$ ) emission  $(n, p)$ , generally occur less frequently than the major  $(n, \gamma)$  reactions, but have a much more significant effect on materials properties. Even at low concentrations, gas particles can have severe life-limiting consequences for materials, with He being a particular problem because, with its low solubility in the crystal lattice, it accumulates at defects, dislocations and at grain boundaries, leading to swelling or embrittlement.

In fusion, the issue of gas production is likely to be a more significant problem than in fission because of the higher neutron fluxes and higher average neutron energies. For example, in figure 1 where a fission spectrum for a fuel assembly of a 3.8 GWt (gigawatts of thermal power) LWR-P4 reactor in Paluel, France, is compared to a fusion spectrum computed for the first wall (FW) of the 3.0 GWt DEMO concept reactor described later, the fluxes of neutrons per lethargy interval<sup>‡</sup> are greater in the fusion spectrum at all but thermal energies. Having said that, the room temperature, homogenous modelling employed for the DEMO concept does not fully realise the thermal part of the neutron flux, and so in reality the fusion spectrum may also be higher in this region as well. Furthermore, whereas the bulk neutron energy in fission is in the 2 MeV range, for every deuterium-tritium fusion reaction in the plasma a 14.1 MeV neutron is produced.

Many of the gas-producing nuclear reactions exhibit cross section thresholds, which means that for incident neutrons below a particular energy the reaction either does not occur or has a very low probability. Thus, in fusion, while the higher neutron fluxes compared to fission would increase the total number of reactions in irradiated components, the larger fraction of neutrons at higher energies would also tend to raise the proportion of those reactions which lead to helium and hydrogen gas production.

This paper describes the latest results from neutron-induced transmutation calculations for fusion-relevant irradiation conditions. In particular, we extend our earlier work [1] to the issue of transmutation and gas production as a function of component position within a conceptual design for DEMO – a demonstration fusion power-plant. We also develop a simple model for the accumulation of helium at

<sup>‡</sup> a lethargy interval is the standard measure for spectra of this type, and is equal to the natural logarithm of the ratio of a given energy-interval's upper bound to its lower bound. The total flux in the interval is divided by the resulting value to give flux per lethargy interval, which is plotted in figure 1 and elsewhere as a step function against the interval bounds.

grain boundaries and, using the transmutation response data, estimate the timescales associated with embrittlement of different materials in a realistic fusion environment.

## 2. Neutron-induced transmutation of materials

In a previous study [1], we considered the transmutation response of various materials under identical first wall conditions for both a power plant design (PPCS model B [2]) and for the ITER device, which is presently under construction. While this provided significant insight into the differing behaviour of materials under neutron irradiation, particularly with regard to He/H gas production, it is important to appreciate the limitations of the approach. Specifically, not all the components of a fusion reactor will experience the same flux and spectrum of neutrons as that seen in the first wall (FW) region. In fact, the FW environment will be the worst in terms of transmutation and gas production due to the high neutron fluxes and energies, and conditions elsewhere may be significantly different. Below we investigate how the neutron-irradiation characteristics change as a function of position in a recent design for a demonstration fusion power plant ('DEMO') and calculate the implications for transmutation and gas production in the materials relevant to a particular position in the structure of the reactor.

### 2.1. Geometry dependence of neutron flux and energy spectrum

Figure 3 shows neutron spectra calculated for different regions of a recent DEMO design, developed at CCFE in 2009, for the DEMO experimental reactor, which is planned as the last step after ITER before progression to commercial fusion reactors. This particular design is helium cooled with a Li/Be tritium breeding blanket and a W divertor. Eurofer is the primary in-vessel structural steel. A model geometry of the design (Figure 2) was created using the HERCULES code [3], and neutrons were transported through it using the MCNP code [4]. Only the major structures were included in the design, with homogeneous material compositions taken as the average composition of all of the materials present in a particular component. This means that, for example, the helium cooling pipes are not modelled explicitly, but rather the He is included in the overall composition of the surrounding region. This homogeneous approach is often used in neutron-transport ('neutronics') scoping calculations, and is considered accurate in most circumstances. However, once the design of DEMO is specified in greater detail, a fully heterogeneous model can be employed to refine the predictions.

To increase the speed of the calculations and, more specifically, to reduce the time needed to reach statistically converged neutron spectra, the radial symmetry of the vessel was utilized to model only a 90° segment of the vessel with reflecting planes, and with the neutron fluxes correctly weighted to reflect the fact that only a quarter of the neutron-generating fusion plasma was represented. A sufficient number of neutron trajectories were tracked to obtain adequate sampling of the neutron-spectra in the regions of interest. The flux results from MCNP, which are given in units of neutrons per square centimetre ( $\text{n cm}^{-2}$ ) per source neutron  $n_s$ , were then multiplied by  $9.576 \times 10^{20} n_s \text{ s}^{-1}$  corresponding to the 2.7 GW expected thermal power output of DEMO, assuming 17.6 MeV energy output per fusion reaction, producing one 14.1 MeV neutron. Note that extra heat is generated by the exothermic nuclear reactions in the blanket, to give a total of 3.0 GW of thermal power output.

Figure 3a, which shows the absolute variation in neutron spectra as a function of depth into the equatorial region of the FW and beyond (position A in figure 2), demonstrates that both the energy profile and fluxes change dramatically over relatively short distances. For example, the flux at the inner-edge of the blanket region, immediately behind the 2 cm FW of steel, at a total depth of 2–3 cm, is not very different from the flux in the FW itself. However, as the neutrons pass deeper into the blanket they become heavily moderated due to the high concentration ( $\sim 74$  atomic %) of Be, and thus the neutron spectrum is very different. In turn, this promotes neutron absorption, particularly by  ${}^6\text{Li}$  ( $\sim 7$  atomic % in the blanket for tritium breeding). As a result, by the outer-edge of the 60 cm-thick blanket in this model, situated at the total depth from plasma face of 57–62 cm, the flux at most energies has fallen by an order of magnitude or more, and the total flux has dropped from  $8.1 \times 10^{14} \text{ n cm}^{-2} \text{ s}^{-1}$  in the first centimetre of the equatorial blanket at position A, to  $3.9 \times 10^{13} \text{ n cm}^{-2} \text{ s}^{-1}$  in the final five cm – a drop of more than 95%.

Within the divertor, on the other hand, the neutron flux and spectrum shows significant variation as a function of position, as well as depth (see figure 3b). At point E in figure 2, the total flux in the 2 cm layer of pure W divertor armour and in the 10 cm layer behind it, containing 20 weight % cooling He as well as W (‘divertor structure’ in figure 2), is approximately twice as high as that in the same layers at G –  $7.1 \times 10^{14} \text{ n cm}^{-2} \text{ s}^{-1}$  and  $5.6 \times 10^{14} \text{ n cm}^{-2} \text{ s}^{-1}$  at E in the armour and structure, respectively, versus  $3.6 \times 10^{14} \text{ n cm}^{-2} \text{ s}^{-1}$  and  $2.4 \times 10^{14} \text{ n cm}^{-2} \text{ s}^{-1}$ , respectively at G.

Note that in figure 3(b) the high concentration of W in the divertor causes a visible self-shielding effect in the lower-energy regions of the neutron spectra. The giant resonances in the neutron-capture cross sections of W produce a much-reduced flux at energies below the resonances [1], leading to the troughs in the spectra around 10 eV. In the divertor, this does not cause a problem, but it could have a significant impact on tritium breeding if too much tungsten, in the form of pure material, say as plasma-facing tiles, or as an alloying component in steel, is used near the blanket because an important contribution to breeding are precisely the population of low energy neutrons in the blanket that would be suppressed by self-shielding. Fortunately, the relatively small self-shielding produced by the 1.1 weight % of W in the Eurofer [5] of the FW, which causes the two minor troughs either side of 10 eV in some of the spectra of figure 3a, is unlikely to have a significant impact on tritium breeding. The effect of tungsten plasma-facing tiles on the spectrum of neutrons reaching the tritium breeding blanket is not considered here.

As is commonly done to aid interpretation of irradiation conditions, we have also calculated the displacements per atom (dpa) per second corresponding to the neutron spectra and fluxes obtained above. Energy-dependent total dpa cross sections were computed using an early version of the NJOY [6] nuclear data processing system. The product of reaction cross section and the energy transferred to lattice atoms that can produce displacements resulting from the said reaction [7] was summed over all reactions onto the naturally occurring isotopes of each element to give the displacement kerma cross section as a function of incident neutron energy  $E_n$ :

$$\sigma_d(E_n) = \sum_j \sigma_j(E_n) E_j(E_n), \quad (1)$$

where  $\sigma_j$  is the collision cross section in barns (1 barn =  $10^{-24} \text{ cm}^2$ ) of reaction  $j$  taken from the European Fusion File (EFF-1), and  $E_j$  is the transferred energy from

the reaction at the given energy computed via a modified version of the Lindhard [8] partition function [7]. Using the modified Kinchin-Pease method of Norgett, Robinson, and Torrens [9] (the ‘NRT’ method), the NRT dpa cross section at energy  $E_n$  is then calculated in units of NRT dpa·barns as:

$$\sigma^{dpa}(E_n) = \frac{0.8\sigma_d(E_n)}{2E_d}, \quad (2)$$

where  $E_d$  is the average displacement threshold for atoms in the material. The estimated values of  $E_d$  for pure materials used in the present work were 31 eV for Be, 40 eV for Fe, Cr, V, Nb, and Zr, 60 eV for Mo, and 90 eV for W and Ta [10]. Note that in real fusion components these elements will mainly be present as part of alloys where the threshold displacement energies could be quite different, but for the present the calculations are restricted to the equivalent NRT dpa in pure materials.

For each neutron spectrum and flux, the damage rate expressed in NRT dpa per second was calculated by collapsing the group-wise neutron flux spectrum with the total NRT dpa cross section for a given material computed using an identical neutron-energy group structure:

$$\text{NRT dpa per second} = \sum_i^{N_g} \phi_i \sigma_i^{dpa}, \quad (3)$$

where  $N_g$  is the total number of energy groups (175 for the NRT dpa calculations),  $\phi_i$  is the total flux in group  $i$  with units of neutrons  $\text{cm}^{-2} \text{s}^{-1}$ , and  $\sigma_i^{dpa}$  is the total NRT dpa cross section for the group.

Here it is important to understand the limitations of the NRT dpa estimates discussed above. The NRT dpa values (referred to subsequently as dpa values) do not take into account the time-evolution of radiation damage in the materials, such as recombination, migration, and coalescence of radiation defects, and in this sense are *not* a measure of radiation damage and do not give any direct information about changes to the microstructure or material properties. Instead, they represent an atom-based approximate measure of the irradiation exposure of the material to the fusion neutrons [11].

The resulting dpa per second defect production rate for one material can be quite different to that in another material under the same irradiation conditions because of differences in the cross sections of neutron reactions. For example, figure 4 gives the variation in dpa per year as a function of depth into the FW at A in figure 2 for the main elements considered in this study. Recall, that, for simplicity, here and elsewhere we are only calculating the dpa values that would result from irradiation of pure materials under the chosen neutron spectrum. The defect production dpa/year rate falls off rapidly with depth for all materials, but is significantly higher in Fe and Cr than in either Be or W. For example, in the 2 cm FW layer at A, the dpa/year is 14.4, 15.0, 7.2, and 4.4 in Fe, Cr, Be, and W, respectively. Note that the assumption of pure elemental materials for the dpa calculations has a further consequence here – we do not account for the compositional changes, either elemental or isotopic, that take place over time. In reality, even in a pure material the defect production dpa per second rate may change as some of the initial atoms are transmuted. However, under the relatively low burn-up rates explored here, the difference between the dpa rate in the pure material and the mixed composition that is created under irradiation will only be very minimal.

## 2.2. Influence on transmutation and gas production

The calculated neutron spectra and total fluxes have been used as input to the inventory code FISPACT [12], which simulates both the evolution in activation and the burn-up (transmutation) of different materials under neutron irradiation. FISPACT requires an external library of reaction cross sections, which is collapsed (or convoluted) with the neutron spectrum, as well as decay data. For the present work we have employed the 2003 version of the European Activation File (EAF) [13], which is the dedicated library compiled specifically for fusion-relevant calculations with FISPACT.

In the earlier analysis [1] the transmutation of different materials was compared using identical irradiation conditions, which in that case were those expected in the FW of a conceptual power plant. Here, we consider the effect on Fe, W, and Be as function of position in the regions of DEMO where they are most likely to be employed within a fusion reactor. Note that, for W, we employ the self-shielding correction-factors obtained in [1] and apply them to the FISPACT calculations. Other materials, such as Cu and SiC, are present in significant quantities in several power plant concepts (SiC, for example, is often proposed as an alternative FW material), but the present calculations are restricted to the three materials that form large structural components in the DEMO model investigated here.

**2.2.1. Fe** The gas production in bulk Fe, as the major constituent of steels, will be a major factor in determining the lifetime of near-plasma component in fusion reactors, and so deserves special attention. Note that chromium (Cr), which is likely to represent around 10% of the composition of reduced activation steels being proposed for fusion applications, has a very similar transmutation profile to Fe, and so the gas concentrations levels calculated for pure Fe are a very good match to those expected in such steels.

Figure 5 shows how the concentration of He and H produced under irradiation varies as a function of position in the FW of the DEMO model. The irradiation times considered here and elsewhere in this work are full-power years, and no attempt has been made to account for maintenance down-times, and other factors determining the availability of the power plant. The dpa/year rates for pure Fe at each of the four positions have also been calculated. The profile of the neutron spectra averaged over the 2 cm FW at positions A–D in figure 2 are all very similar. However, the total flux in these different regions of the FW does vary somewhat, with the total flux being  $8.25 \times 10^{14} \text{ n cm}^{-2} \text{ s}^{-1}$  at A,  $6.97 \times 10^{14} \text{ n cm}^{-2} \text{ s}^{-1}$  at B,  $8.04 \times 10^{14} \text{ n cm}^{-2} \text{ s}^{-1}$  at C, and  $7.94 \times 10^{14} \text{ n cm}^{-2} \text{ s}^{-1}$  at D. We note that all of these fluxes are lower than the  $1.04 \times 10^{15} \text{ n cm}^{-2} \text{ s}^{-1}$  total flux calculated for the conceptual power plant model that was used for the scoping calculations reported in [1], which explains why the gas concentrations in figure 5 are at least 30% lower than those given there (see table 3 of [1]).

The variation in He and H production rates in Fe (figure 5), particularly between position B, at the top of the vessel, and the other three, appears to be greater than that suggested by comparing the ratios of the total flux in the different FW regions. Both the  $^{56}\text{Fe}(n, \alpha)^{53}\text{Cr}$  and  $^{56}\text{Fe}(n, p)^{56}\text{Mn}$  reactions, which are responsible for most of the He and H produced in pure Fe, respectively, are threshold reactions. Only for neutron energies above the threshold does a reaction become possible, and for the  $(n, \alpha)$  and  $(n, p)$  reactions on  $^{56}\text{Fe}$  the thresholds are at approximately 3.7 MeV and 2.9 MeV,

respectively [13]. Examining the spectra for the different positions more closely it is apparent that at B in figure 2 there is a noticeable reduction in the neutron energies above 1 MeV (see figure 6), which is precisely the range over which the gas production reactions become more likely, and so helium and hydrogen production at B is reduced. After five full-power years, for example, the He concentration in the FW at B has only reached 365 atomic parts per million (appm), while in the FW at the other three positions the He concentration after five years is 709, 734, and 586 appm for positions A, C, and D, respectively. The reduction in frequency of the threshold reactions at B also accounts for the greatly reduced dpa/year rate in pure Fe – in regions A–C the dpa/year is of the order of 13–14, while at B it is less than 10 dpa/year.

As a function of depth into the vessel from the plasma at position A we have already seen that neutron irradiation conditions change dramatically between the plasma facing wall and the outer edge of the blanket (see figure 3), with the total flux and dpa/year reducing and the energy spectrum becoming softer. Inventory calculations reveal that these changes cause the He (and H) production levels to fall significantly. For example, from the results presented in figure 7 for the He concentration after 5 full-power years, the He concentration in the FW is around 700 appm at A, while in the final 5 cm of the blanket, which is at a total depth from the plasma of 57–62 cm, the amount of He only reaches 3 (three) appm. Over the same range, the dpa rate in pure Fe falls from 72 dpa/year in the FW to only 1 dpa/year at the outer edge of the blanket (figure 4). Such a profound change in both gas production and dpa rates could have important consequences in terms of He-induced brittleness in Fe and hence steels.

However, the neutron spectra calculated by MCNP do not take into account time-dependent compositional changes in materials, *i.e.* each neutron is propagated through the model as though it were the first. For the blanket, in particular, which is solid-type helium-cooled pebble-bed (HCPB) concept in the model, the compositional changes that take place as a result of nuclear reactions, could lead to a significant evolution (in time) in the neutron irradiation conditions. Neutrons entering the blanket are moderated by Be and subsequently absorbed efficiently by Li to produce tritium. Initially, this happens predominantly in the first few centimetres of the blanket, leading to the changes in neutron spectrum and flux, and thus gas production observed in the present calculations. Subsequently, as the Li, and to a lesser extent the Be, are burnt-up (transmuted) in these near-plasma regions, fewer of the neutrons are absorbed and so the flux at greater depths can increase in certain energy ranges. The cycle then repeats as the Li in deeper regions of the blanket is depleted, and so on. Hence, it is possible that if this time evolution were taken into account the dpa/year values and He concentrations in the near-plasma regions of the blanket would be reduced in a given time-frame, while in the outer regions they would increase. Such a time evolution can be investigated by coupling MCNP to an inventory code (such as FISPACT), which updates the material compositions in the model at frequent intervals, thus allowing the changes in neutron flux and spectra to be quantified. This method has recently been applied by Packer *et al* [14] to investigate how the tritium-breeding inventory evolves in the DEMO blanket.

Another important observation from figure 7, is that care should be taken when using the spectra averaged over large regions of reactor vessels. While the results for the volume-averaged flux in the FW at A are in broad agreement with the finer, 0.5 cm, divisions because the FW is only 2 cm thick, for the 60 cm blanket the average is a poor representation, predicting only 84 appm after five years, compared



to 600 appm in the first 1 cm of the blanket. The difference between 84 and 600 appm would be measurable as far as the structural properties of Fe (and steels) is concerned – implanted He concentrations in the range of 400 appm are known to cause significantly more pronounced embrittlement of fission neutron-irradiated steels compared to those exposed to fission neutrons alone [15]. Here we note that fission neutrons on their own do not generate appreciable amounts of transmutation gas products in the materials.

*2.2.2. W* While W (tungsten) will be present throughout a typical reactor vessel as small concentrations in most steels, including around 1.1 weight % in Eurofer steel, it will be used in an almost pure form primarily in the high heat-flux regions, such as the divertor, because of its high melting-point, high thermal-conductivity, and resistance to sputtering and erosion [16]. In many reactor designs, including the model for DEMO discussed in the present work, it is also assumed to be the main material in both the armour and structural components of the divertor, while in some power plant concepts it is also considered for the FW armour layer [2]. As a small part of steels, the transmutation-related gas production from W is unlikely to be consequential, although its transmutation to other elements, such as Re or Os, may cause non-negligible changes in structural properties, but in those regions where W is the chief element, a quantification of gas production is vital.

The results from inventory calculations reveal that the concentration of He (and H) produced from pure W can vary significantly, even within the same layer of the divertor. We find that the amount of He produced in the divertor armour (the first 2 cm in the divertor close-up in figure 2) after a 5-year full-power irradiation varies from 15 appm at position E, to less than 1 (one) appm at G – an order of magnitude difference – although both could be viewed as negligible. A similar variation with position is also obtained for the 10 cm layer behind the armour (a mixture of W and He, called the ‘divertor structure’ in figure 2). These findings are summarised in figure 8a. Note that for H, by comparison, the variations with position are of a similar order, although the level of production overall is roughly twice as great as that for He.

Figure 8 also demonstrates that helium production from W is greater in the FW than in the divertor. For the present DEMO model, the FW layer is very thin, meaning that it is almost transparent to neutrons. Therefore, it is realistic to assume that the fluxes and energy spectra obtained from MCNP calculations with a steel FW on DEMO are very close to those that would be found if the FW were W instead. The observed variation in transmutation response between the FW and the divertor is primarily due to differences in total neutron flux in the FW compared to the divertor, with for example, a flux of  $8.25 \times 10^{14} \text{ n cm}^{-2} \text{ s}^{-1}$  in the 2 cm FW at A producing 4.4 dpa/year vs.  $7.51 \times 10^{14} \text{ n cm}^{-2} \text{ s}^{-1}$  giving 3.4 dpa/year in the divertor armour at E. However, the changes to the profile of the neutron spectra is also a contributing factor. Comparing figures 3a and 3b, we see that flux levels in the few MeV range are significantly lower in the divertor, which is precisely the region of the energy spectrum that contributes to many of the threshold gas-producing reactions on isotopes of W.

Similarly there are significant reductions in Re concentration between the FW and the divertor (figure 8b). After five years in the FW at A, Re reaches a concentration of 30000 appm (3 atomic %), which is broadly in line with the findings for the FW of PPCS-B in [1] after taking into account the reduction in total flux. However, in the divertor armour at position E, Re only reaches a concentration of around 10000 appm (1 at.%) on the same timescale. This factor of three reduction is much greater than the  $\sim 1.1$  ratio between the total fluxes in the FW and divertor.

The primary reactions contributing to the production of Re, or indeed heavier elements such as Os, from W are the  $(n, \gamma)$  reactions, which normally have a cross section that is proportional to  $1/\sqrt{E_n}$  at low neutron energies  $E_n$ . In figure 3 the spectra associated with the divertor regions of the DEMO model have a profile that is much less moderated than that in the FW, which has a large contribution from moderated neutrons that have back-scattered from the Be/Li blanket. Thus, the proportion of neutrons at the lower energies is reduced in the divertor, which leads to a smaller probability for the  $(n, \gamma)$  reactions (compared to other nuclear reactions), and so the production of Re is disproportionately lower.

On the other hand, figure 8c suggests that the changes in energy-spectrum profile between the FW and divertor do not particularly alter the rate at which W transmutes into Ta (tantalum). In the FW at location A, the Ta concentration is calculated to be 5470 appm after a five-year exposure, while in the divertor armour at E it is 4940 appm. The ratio between these two values is exactly the same as the ratios of the total flux ( $\sim 1.1$ ), suggesting that this is the main reason for the variation, despite the apparent differences in the energy spectra shown in figure 3.

This is somewhat surprising because many of the nuclear reactions on W that produce Ta, either directly or indirectly, including  $(n, 2n)$ , have thresholds. Based on the high-energy regions of the spectra in figure 3, one might expect these threshold reactions to be reduced in the divertor, leading to a reduction in Ta production compared to the FW that is greater than a simple scaling of the total fluxes. Since this is not the case further investigation is needed, but it illustrates the subtle complexities associated with neutron-transport and inventory calculations of this kind.

**2.2.3. Be** Beryllium, as the primary constituent of the blanket in the present DEMO model, has been found previously [1] to produce significant concentrations of He under neutron irradiation. For the present model, the inventory calculations indicate He concentrations in Be after 5-year irradiations of between 19300 appm in the first 1 cm of the equatorial blanket at position A in figure 2, to only 200 appm in the final 5 cm (see figure 9). As noted previously, this extreme range of values, which is even greater than the drop observed for Fe in figure 7, is likely to be time-dependent because the neutron-energy spectrum in different regions of the blanket will evolve as the Li is depleted. However, the large difference, which on shorter timescales equates to approximately 320 appm He per month within the inner 1 cm of blanket, and around 3 appm per month in the outer 5 cm, is likely to produce non-homogeneous changes to structural and mechanical properties across the full depth of the blanket. For instance, Be is known to swell significantly under neutron irradiation, due to the generation of helium in the bulk of the material [17, 18], and a variation in swelling rates would produce significant stress differentials in components.

Note that, by comparison, hydrogen gas production in Be is around two orders of magnitude less than for He, with, for example, only 475 appm produced in five years of reactor operation under the conditions calculated for the first centimetre of the DEMO blanket at A.

### 3. Modelling of He accumulation at grain boundaries

The calculations described in the foregoing section produce quantitative estimates of the He production rates under any neutron-irradiation conditions. However, without knowing what constitutes ‘too much’ He production, it is difficult to fully appreciate

the mechanical or structural consequences (or the absence of those) of a particular level of He accumulation. By applying some straightforward concepts and simplifying assumptions, we can attempt to estimate the critical He densities in grains that could lead to the grain boundary destabilization that characterizes embrittlement. Subsequently, the timescales required to produce these densities can be approximated using the neutron transport and inventory calculations, thus giving insight into the differences in component lifetime that could result from using different materials.

Assuming a spherical grain shape in a crystalline material, the total number of He atoms  $N_{\text{He}}$  within a grain of radius  $R$  is approximated by

$$N_{\text{He}} \approx \frac{4}{3}\pi R^3 n G_{\text{He}}, \quad (4)$$

where  $G_{\text{He}}$  is the atomic concentration of He atoms in appm, and  $n$  is the atomic density of the material ( $\text{cm}^{-3}$ ), which are approximated for a given element using atomic weights and room temperature densities (see Table 1). If every He atom produced in a given grain is available for migration to the grain boundary (GB), then  $\nu_{\text{He}}$ , the surface density of He at the GB satisfies

$$4\pi R^2 \nu_{\text{He}} = \frac{4}{3}\pi R^3 n G_{\text{He}}.$$

Therefore,

$$\nu_{\text{He}} = \frac{R}{3} n G_{\text{He}}. \quad (5)$$

In a real grain there are likely to be internal obstacles, such as dislocations and vacancy clusters, that trap some of the He atoms, preventing it from reaching the grain boundaries. The presence of such traps is neglected here for simplicity.

The grain structure of a material destabilizes (*i.e.* the grain boundaries fail) if the stored energy associated with He accumulated at boundaries becomes greater than or equal to the energy required to make all the boundaries become free surfaces. If we now approximate the energy of solution of a He atom at a boundary by its upper bound, the energy of solution for a He atom in a perfect lattice  $E_{\text{He}}^{\text{sol}}$ , then

$$E_{\text{He}}^{\text{sol}} \nu_{\text{He}}^c \approx 2\varepsilon_{\text{surf}}, \quad (6)$$

where  $\varepsilon_{\text{surf}}$  is the surface energy per unit area for the given material, which is multiplied by two here because each GB is associated with two grains. Here we acknowledge that at certain boundaries, corresponding to particular orientations of neighbouring grains, solution of He is likely to be more favourable than in the grain bulk, but certainly not less so. Hence  $\nu_{\text{He}}^c$  is the critical surface density of He atoms required to bring-about boundary destabilization. Once  $\nu_{\text{He}}^c$  is known, the critical bulk He concentration  $G_{\text{He}}^c$  is readily found from equation Equation (5):

$$G_{\text{He}}^c = 3\nu_{\text{He}}^c / Rn. \quad (7)$$

Table 2 shows the values of  $\nu_{\text{He}}^c$  and  $G_{\text{He}}^c$  calculated for various elemental materials being considered for fusion applications. Here we have used the estimates of surface and He-solution energies given in Table 1. Since we do not know the specific grain orientations associated with fracture, the values of surface energy given in the table are estimated as the average of experimental values reported by Vitos *et al* [19]. Similarly, for the He-solution energies, we have taken the average of DFT calculations for various positions of the He atom in the lattice from [20, 21, 22, 23].

The  $G_{\text{He}}^c$  values in Table 2 show significant variation between different elements. Note that  $G_{\text{He}}^c$ , as defined here, is strongly dependent on the parameters  $E_{\text{He}}^{\text{sol}}$ ,  $\varepsilon_{\text{surf}}$ , and

$n$ , and so refinement of the approximate values for these quantities might significantly alter the lifetime predictions.

Even though Zr (zirconium) has the lowest He solution energy (2.83 eV), it also has a relatively low atomic density, leading to the greatest critical bulk He concentration  $G_{\text{He}}^c$  because  $G_{\text{He}}^c \propto 1/n$ . Be, on the other hand, has the highest atomic density  $n$ , and so, unsurprisingly, has the lowest  $G_{\text{He}}^c$  value and is likely to be more susceptible than most to He-induced grain-boundary embrittlement.

With these  $G_{\text{He}}^c$  values we can now estimate the lifetime of various materials in a fusion reactor based on the time taken to produce the critical He concentration at grain boundaries under neutron irradiation. To allow a direct comparison between different materials, the critical lifetimes  $t^c$  and equivalent integral values of NRT dpa given in Table 2 were computed for identical irradiation conditions in each case. The MCNP-calculated neutron-transport result for the 2 cm DEMO FW at position A (see figure 2) was used, which has the neutron spectrum shown in figure 6 and a total flux of  $8.25 \times 10^{14} \text{ n cm}^{-2} \text{ s}^{-1}$ . Note that in the case of inventory calculations, there is not necessarily a linear relation between the  $G_{\text{He}}^c$  and  $t^c$ , because of the subtleties associated with transmutation. For instance, as an element is burnt-up, the products may be more (or less) prone to He production, leading to an acceleration (or deceleration) in accumulation as time progresses.

Beryllium, with its low critical density  $G_{\text{He}}^c$  and high He production rates, has the lowest estimated lifetimes and dpa before embrittlement; the predicted lifetime for a grain size of  $5 \mu\text{m}$  is only 4 days, corresponding to 0.08 dpa. Meanwhile Ta, and to a lesser extent W, have high critical densities and low He production rates, implying long lifetimes; more than 200 years and 1000 dpa in the case of the small  $0.5 \mu\text{m}$  grains. Even for the large,  $5 \mu\text{m}$  grains, the predicted irradiation lifetime for W is 16 years or 71 dpa, suggesting that, even under FW conditions, the issue of He embrittlement might not be a cause for concern. On the other hand, Mo, which could conceivably be an alternative to W as a divertor or FW material, has much higher He production rates, so the predicted lifetimes, at 1.5 years and 16 years for the large and small grains, respectively, are much shorter, even though the required  $G_{\text{He}}^c$  are similar to those in W.

More crucially, however, the lifetimes predicted for the two grain sizes in Fe go from the problematic at 4 months or 5 dpa for a  $5 \mu\text{m}$  grain, to almost commercially viable at 4 years or 57 dpa in the limit of small,  $0.5 \mu\text{m}$  grain (recent estimates put a commercially viable lifetime of 5 years on the FW of a power plant [24]). This illustrates how critical material grain size might be in defining the lifetime of fusion-reactor components.

Despite the roughness of the approximations made in the preceding arguments, the results demonstrate that materials exposed to high neutron fluxes and energies can have vastly differing evolution in properties (in this case grain-boundary embrittlement). Further work in this area, including investigations of the influence of He traps (such as dislocations and voids), interaction with hydrogen, preferential accumulation, and temperature effects, are needed to provide accurate predictions of He-limited component lifetimes. The present work is a first step in this investigation.

#### 4. Summary

The combined MCNP-based neutron transport simulations and FISPACT-based inventory calculations for the neutron-irradiation conditions expected in the DEMO

concept reactor demonstrate that both He and H accumulation rates, and transmutation rates in general, can vary dramatically, even within the same component of a fusion reaction. In Fe, the production of He is likely to be significant and severe within the first wall of a reactor, but will fall off rapidly in deeper radial locations, through the tritium-breeding blanket, due to the effective moderation and absorption of neutrons required for efficient production of tritium ( $^3\text{He}$ ). By the time neutrons reach the outer vessel components, such as the shield and vacuum-vessel walls, the quantities of He predicted are at such a low level that they are unlikely to pose a serious threat to the structural integrity of components.

In W the predicted gas concentrations are probably too low to have any impact on component lifetime, especially given the results from the modelling of embrittlement, which show that W is one of the best materials in the respect of how much He the grain-boundaries can absorb before failure. At the same time, further work is needed to assess the acceptable levels of other transmutation products in W, such as Re, Ta, and Os, because these can reach non-negligible levels, and might cause undesirable changes to material properties.

In Be, on the other hand, the inventory calculations confirm the previous findings [1], and show that He can be produced in significant quantities in the inner regions of the blanket. Initially, the production rate tails off rapidly as the conditions change through the blanket, so that by its outer edge the He concentrations are roughly two orders of magnitude smaller than at the inner, near-plasma edge. However, as noted, this could vary in time as the Li in the tritium-breeding blanket is depleted, reducing the neutron absorption rate. Eventually, as the DEMO design is refined and finalized, fully-fledged fuel-cycle calculations of inventory burn-up will be needed to complement and improve not only the findings for Be, but additionally for other materials, whose burn-up will also be strongly influenced by the changing environment within the blanket.

Finally, by applying suitable assumptions, some basic modelling of the grain boundary embrittlement of various different candidate fusion materials reveals that the range of expected lifetimes of components in fusion reactors might vary greatly as a function of the particular materials (elements) chosen in their construction. For instance, structural Fe, under suitable conditions, may adequately withstand He embrittlement on commercially viable timescales, whereas Be almost certainly would not; unless a way can be found to mitigate the swelling and embrittlement caused by the vast quantities of He it produces under neutron-irradiation.

## Acknowledgments

The authors gratefully acknowledge helpful discussions with R.G. Odette, M. Rieth, T. Yamamoto, and P. Karditsas. This work, partly funded by the European Communities under the contract of association between EURATOM and CCFE, was carried out within the framework of the European Fusion Development Agreement. The views and opinions expressed herein do not necessarily reflect those of the European Commission. This work was also part-funded by the RCUK Energy Programme under Grant No. EP/I501045. S.L. Dudarev acknowledges support from the EURATOM staff mobility program.

[1] Gilbert M R and Sublet J -Ch, 2011, *Nucl. Fus.*, **51** 043005

[2] Maisonnier D, Cook I, Sardain P, Boccaccini L, Bogusch E, De Pace L, Forrest R, Giancarli L,

- Hermesmeier S, Nardi C, Norajitra P, Pizzuto A, Taylor N, and Ward D, 2005, *Fusion Eng. Des.*, **75–79** 1173–1179
- [3] Karditsas P J HERCULES: a code system for Fusion Power Plant Analysis; unpublished UKAEA (now CCFE) Fusion Report 2000
- [4] Brown F B, Barrett R, Booth T, Bull J, Cox L, Forster R, Goorley J, Mosteller R, Post S, Prael R, Selcow E, Sood A, and Sweezy J, 2002, *Trans. Am. Nucl. Soc.*, **87** 273
- [5] Rieth M, Klimenkov M, Materna-Morris E, and Möslang A Review of the physical metallurgy of EUROFER, 2008; Final report, EFDA task TW6-TTMS-007 D10
- [6] MacFarlane R E and Muir D W The NJOY Nuclear Data processing System: Version 91; LA-12740-M (UC-413), Los Alamos National Laboratory Report, October 1994
- [7] Ougouag A M, Wemple C A, and Siclen C D V Displacement Kerma Cross Sections For Neutron Interactions In Molybdenum; INEEL/CON-03-01258, Idaho National Engineering and Environmental Laboratory, April 2004
- [8] Lindhard J, Nielsen V, Scharff M, and Thomsen P V, 1963, *Mat. Fys. Medd. Dan. Vid. Selsk.*, **33** 1–42
- [9] Norgett M J, Robinson M T, and Torrens I M, 1975, *Nucl. Eng. Des.*, **33** 50–54
- [10] Panini G C and Peerani P A Library of Nuclear Response Functions in Vitamin-J Structure; RFL-1, presented at the EFF Meeting, NEA Data Bank, Saclay (Paris), December 1991
- [11] Stoller R E, Calder A F, Osetsky Yu N, and Bacon D J Displacement Cascade Evolution: Neutron Irradiation vs. Ion Near-surface Damage, 2011; Presentation given at the Oxford Materials Ion Irradiation workshop, Oxford, September 2011 (unpublished)
- [12] Forrest R A, FISPACT-2007: User manual, UKAEA FUS 534, 2007
- [13] Forrest R A, The European Activation File: EAF-2003 overview, UKAEA FUS 484, 2002
- [14] Packer L W, Pampin R, and Zheng S, 2011, *J. Nucl. Mater.*, **417** 718–722
- [15] Yamamoto T, Odette G R, Kishimoto H, Rensman J W, and Miao P, 2006, *J. Nucl. Mater.*, **356** 27–49
- [16] Nemoto Y, Hasegawa A, Satou M, and Abe K, 2000, *J. Nucl. Mater.*, **283–287** 1144–1147
- [17] Chakin V P, Posevin A O, and Kupriyanov I B, 2007, *J. Nucl. Mater.*, **367–370** 1377–1381
- [18] Möslang A, Pieritz R A, Boller E, and Ferrero C, 2009, *J. Nucl. Mater.*, **386–388** 1052–1055
- [19] Vitos L, Ruban A, Skriver H, and Kollár J, 1998, *Surf. Sci.*, **411** 186–202
- [20] Willaime F and Fu C C, 2006, *Mater. Res. Soc. Symp.*, **981** 0981–JJ05–04
- [21] Ganchenkova M G, Vladimirov P V, and Borodin V A, 2009, *J. Nucl. Mater.*, **386–388** 79–81
- [22] Middleburgh S C and Grimes R W, 2011, *Acta Mater.*, **59** 7095–7103
- [23] Koroteev Yu M, Lopatina O V, and Chernov I P, 2009, *Phys. Solid State*, **51** 1600–1607
- [24] Maisonnier D, Cook I, Sardain P, Boccaccini L, De Pace L, Giancarli L, Norajitra P, and Pizzuto A, 2006, *Fusion Eng. Des.*, **81** 1123–1130
- [25] Lide D R, editor, 2004, *CRC Handbook of Chemistry and Physics* (CRC Press, Boca Raton, Florida) 85th edition

## Tables

**Table 1.** Table of basic quantities.  $\rho^{\text{RT}}$  is density at room temperature (RT),  $n$  is atomic density (see equation Equation (5)),  $E_{\text{He}}^{\text{sol}}$  is solution energy of a He atom, and  $\varepsilon_{\text{surf}}$  is surface energy.

Element	$\rho^{\text{RT}}$ ( $\text{gcm}^{-3}$ ) <sup>1</sup>	Atomic mass (amu) <sup>1</sup>	$n$ ( $\text{cm}^{-3}$ )	$E_{\text{He}}^{\text{sol}}$ (eV)	$\varepsilon_{\text{surf}}$ ( $\text{Jm}^{-2}$ ) <sup>5</sup>
Fe	7.87	55.845	$8.5 \times 10^{22}$	4.43 <sup>2</sup>	2.4
V	6.11	50.942	$7.2 \times 10^{22}$	3.78 <sup>2</sup>	2.6
Cr	7.19	51.996	$8.3 \times 10^{22}$	5.19 <sup>2</sup>	2.3
Mo	10.22	95.940	$6.4 \times 10^{22}$	5.12 <sup>2</sup>	3.0
Nb	8.57	92.906	$5.6 \times 10^{22}$	3.76 <sup>2</sup>	2.7
Ta	16.65	180.948	$5.5 \times 10^{22}$	4.05 <sup>2</sup>	3.0
W	19.25	183.840	$6.3 \times 10^{22}$	5.82 <sup>2</sup>	3.5
Be	1.85	9.012	$1.2 \times 10^{23}$	5.72 <sup>3</sup>	2.2
Zr	6.51	91.224	$4.3 \times 10^{22}$	2.83 <sup>4</sup>	2.0

<sup>1</sup> Data taken from [25].

<sup>2</sup> Averaged values from DFT results in [20].

<sup>3</sup> Averaged values from [21, 22].

<sup>4</sup> Average for bcc crystals from [23].

<sup>5</sup> Averages of experimental values reported in [19]

**Table 2.** Table of calculated critical boundary densities  $\nu_{\text{He}}^c$ , critical bulk concentrations  $G_{\text{He}}^c$  for He in various elements, and the approximate critical lifetimes  $t^c$  in DEMO first-wall full-power time and equivalent integral dpa. Results for two different grain radii  $R$  shown.

Element	$\nu_{\text{He}}^c$ ( $\text{cm}^{-2}$ )	$R$ ( $\mu\text{m}$ )	$G_{\text{He}}^c$ (appm)	DEMO FW $t^c$	dpa <sup>c</sup>
Fe	$6.76 \times 10^{14}$	5	47.8	4 months	4.79
V	$8.59 \times 10^{14}$	5	71.3	1.5 years	25.07
Cr	$5.53 \times 10^{14}$	5	39.9	5 months	6.27
Mo	$7.31 \times 10^{14}$	5	68.4	1.5 years	14.34
Nb	$8.96 \times 10^{14}$	5	96.8	2.5 years	39.99
Ta	$9.25 \times 10^{14}$	5	100.1	21 years	118.92
W	$7.51 \times 10^{14}$	5	71.4	16 years	71.11
Be	$4.80 \times 10^{14}$	5	23.3	4 days	0.08
Zr	$8.82 \times 10^{14}$	5	123.2	4 years	61.99
Fe	$6.76 \times 10^{14}$	0.5	478.1	4 years	57.47
V	$8.59 \times 10^{14}$	0.5	713.2	15 years	250.75
Cr	$5.53 \times 10^{14}$	0.5	398.6	4 years	60.20
Mo	$7.31 \times 10^{14}$	0.5	684.1	16 years	152.97
Nb	$8.96 \times 10^{14}$	0.5	968.2	21 years	335.92
Ta	$9.25 \times 10^{14}$	0.5	1001.2	283 years	1602.62
W	$7.51 \times 10^{14}$	0.5	714.3	244 years	1084.49
Be	$4.80 \times 10^{14}$	0.5	233.0	22 days	0.43
Zr	$8.82 \times 10^{14}$	0.5	1231.7	40 years	619.88



### Figure Captions

Figure 1. Comparison of the neutron-energy spectra in fission and fusion reactors. For fission the average neutron spectrum in the fuel-assembly of a PWR reactor is shown, while the equatorial FW spectrum for the DEMO model in figure 2 is representative of fusion.

Figure 2. The simplified, homogeneous, DEMO model used in MCNP simulations to obtain neutron fluxes and spectra.

Figure 3. Comparison of the neutron-energy spectra in DEMO; (a) as a function of depth into different regions of the containment vessel at the equatorial position (A) in figure 2; and (b) in the first two layers of the divertor as a function of position ((E-G) in 2).

Figure 4. Defect production rates, expressed in dpa per year units for different elements shown as a function of depth into the FW at A in figure 2.

Figure 5. Variation in the (a) He, and (b) H, concentrations in pure Fe as a function of time for the spectra at different FW positions in DEMO – see figure 2. The equivalent dpa/year in pure Fe at each position are also given.

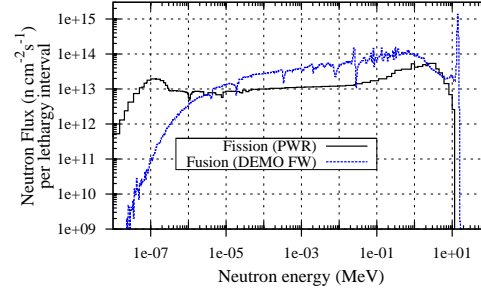
Figure 6. The high-energy part of the neutron spectra for the 2 cm FW layer at four different positions within the DEMO model (figure 2). The slight drop in the flux at B shown here leads to the  $\sim 50\%$  drop in gas production in figure 5.

Figure 7. Variation in He concentration in pure Fe after a five-year irradiation as a function of depth (from the plasma) into the DEMO vessel at (A) in figure 2. Also shown is the total dpa in pure Fe, evaluated by integrating the dpa rates over time, at each depth after five years.

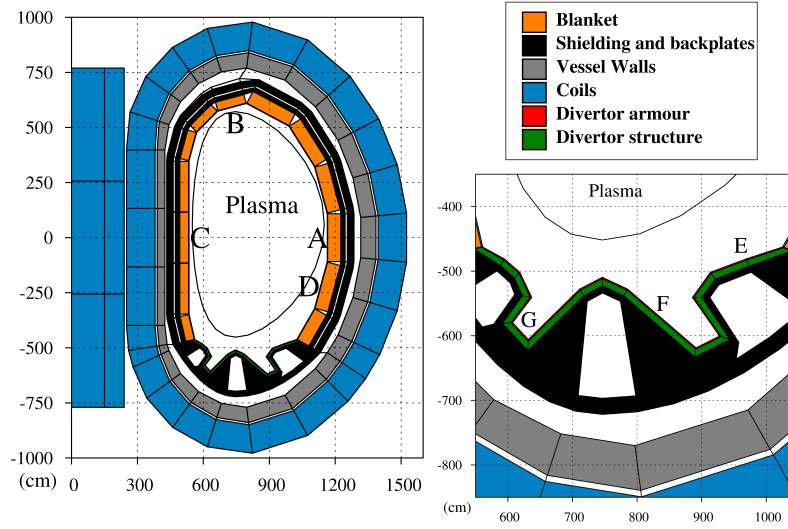
Figure 8. Variation in concentrations of (a) He, (b) Re, and (c) Ta, produced in pure W under neutron irradiation as a function of position (and depth) in the divertor region of the DEMO design (figure 2). In (a) the equivalent dpa/year in pure W are also given for each position.

Figure 9. Variation in He concentration in pure Be after a five-year irradiation as a function of depth into the DEMO blanket at (A) in figure 2. The equivalent dpa in pure Be after five years is also given at each depth

## Figures



**Figure 1.** Comparison of the neutron-energy spectra in fission and fusion reactors. For fission the average neutron spectrum in the fuel-assembly of a PWR reactor is shown, while the equatorial FW spectrum for the DEMO model in figure 2 is representative of fusion.



**Figure 2.** The simplified, homogeneous, DEMO model used in MCNP simulations to obtain neutron fluxes and spectra.

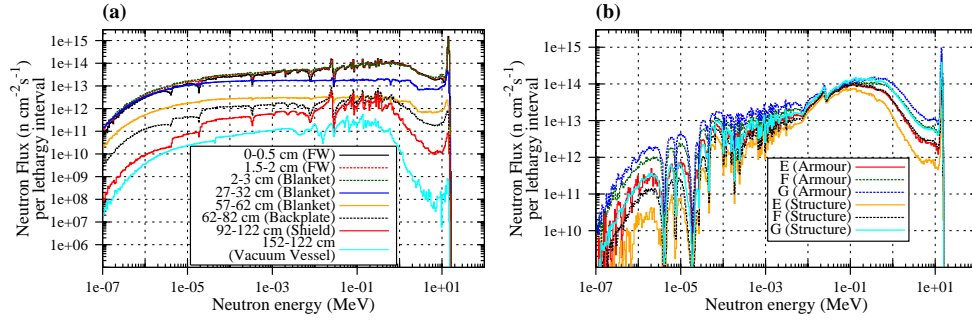


**Figure 3.** Comparison of the neutron-energy spectra in DEMO; (a) as a function of depth into different regions of the containment vessel at the equatorial position (A) in figure 2; and (b) in the first two layers of the divertor as a function of position ((E-G) in 2).

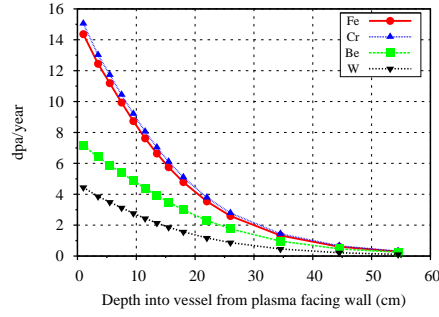


**Figure 4.** Defect production rates, expressed in dpa per year units for different elements shown as a function of depth into the FW at A in figure 2.

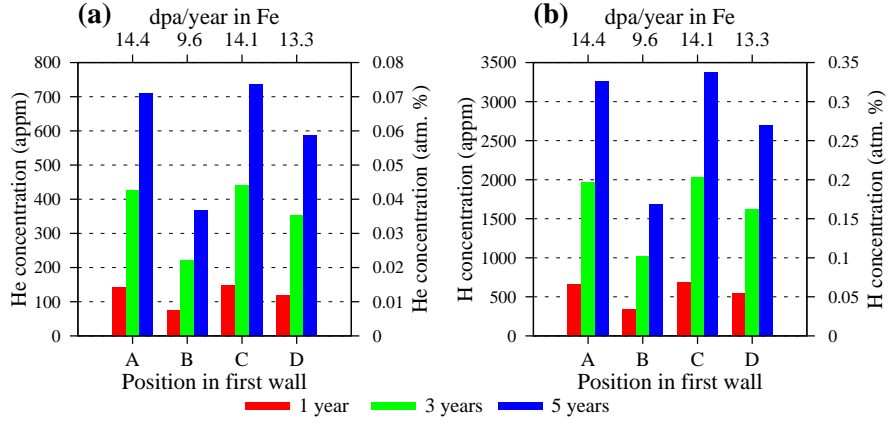


**Figure 5.** Variation in the (a) He, and (b) H, concentrations in pure Fe as a function of time for the spectra at different FW positions in DEMO – see figure 2. The equivalent dpa/year in pure Fe at each position are also given.

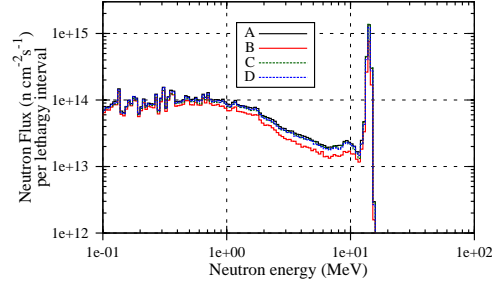


**Figure 6.** The high-energy part of the neutron spectra for the 2 cm FW layer at four different positions within the DEMO model (figure 2). The slight drop in the flux at B shown here leads to the  $\sim 50\%$  drop in gas production in figure 5.

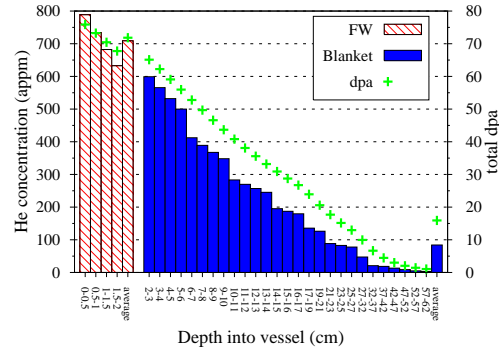


**Figure 7.** Variation in He concentration in pure Fe after a five-year irradiation as a function of depth (from the plasma) into the DEMO vessel at (A) in figure 2. Also shown is the total dpa in pure Fe, evaluated by integrating the dpa rates over time, at each depth after five years.

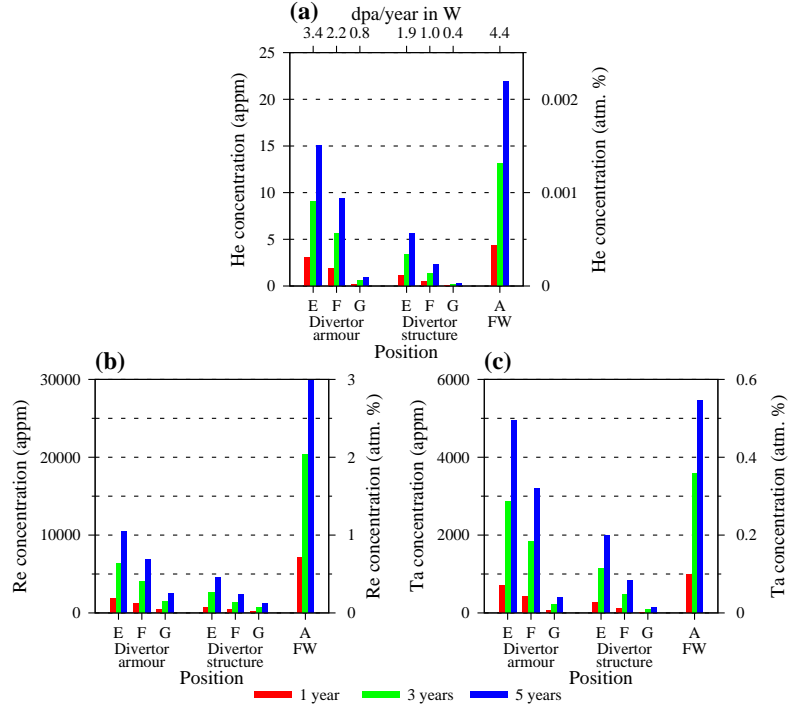


**Figure 8.** Variation in concentrations of (a) He, (b) Re, and (c) Ta, produced in pure W under neutron irradiation as a function of position (and depth) in the divertor region of the DEMO design (figure 2). In (a) the equivalent dpa/year in pure W are also given for each position.

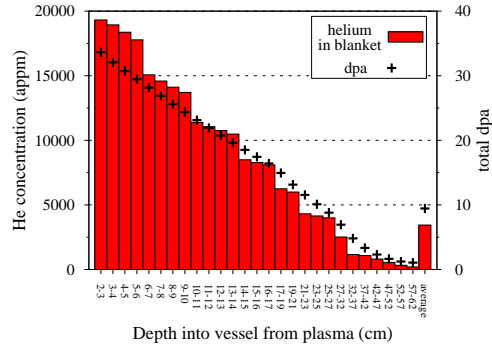


**Figure 9.** Variation in He concentration in pure Be after a five-year irradiation as a function of depth into the DEMO blanket at (A) in figure 2. The equivalent dpa in pure Be after five years is also given at each depth.